https://doi.org/10.1016/j.compgeo.2022.105218

Numerical analysis of time-dependent negative skin friction on pile in soft soils

Rui LIANG[1], Zhen-Yu YIN[2], Jian-Hua YIN[3], Pei-Chen WU[4]

Abstract: The generation of negative skin friction (NSF) induces the additional axial force on the pile, which exerts a detrimental load rather than a beneficial one. However, the effect of soil creep on the long-term development of NSF has remained poorly understood. The study uses numerical analysis to investigate this effect. First, an elasto-viscoplastic model with an enhanced time integration algorithm is successfully implemented into a finite element code. Next, the two-dimensional axisymmetric pile-soil interaction model is established and properly calibrated with a known field case. Finally, parametric studies are conducted to examine different degrees of creep effect on the variation in NSF and neutral plane (NP) within the primary and secondary consolidation periods. According to the findings, a high creep coefficient of the soil results in an increase in NSF and descending trend of the NP. The creep induced delay of NSF is observed attributed to the increase in excess pore pressure during the early stage of consolidation. The NP position varies drastically at the commencement of consolidation when taking creep into consideration. Lastly, the study proposes an exponential prediction model to reflect the time dependence of the location of the NP.

Keywords: soft clay, pile, negative skin friction, neutral plane, creep, finite element method

[1] PhD student, Department of Civil and Environmental Engineering, The Hong Kong Polytechnic University, Hong Kong, China. E-mail address: ruicee.liang@connect.polyu.hk

[2] Professor, Department of Civil and Environmental Engineering, The Hong Kong Polytechnic University, Hong Kong, China. Corresponding author. E-mail address: zhenyu.yin@polyu.edu.hk; Tel: (+852) 3400 8470; Fax: (+852) 2334 6389 (corresponding author)

[3] Chair Professor, Department of Civil and Environmental Engineering, The Hong Kong Polytechnic University, Hong Kong, China. E-mail address: jian-hua.yin@polyu.edu.hk

[4] Research Assistant Professor, Department of Civil and Environmental Engineering, The Hong Kong Polytechnic University, Hong Kong, China. E-mail address: elvis.wu@polyu.edu.hk

1. Introduction

Many tall buildings are supported by piles that have been driven into recently reclaimed soils. The consolidation of soil may lead to a substantial degree of settlement around the pile. Normally, the positive skin friction along the pile, along with the pile toe resistance support the load imposed by the upper structure. However, the downward movement of the soil relative to the pile changes the shear force direction in the pile-soil interface, inducing the negative skin friction (NSF), which has the same direction as gravity. The additional axial force induced by NSF, called drag load, causes extra pile settlement, referred to as down drag (Fellenius, 1989). The drag load is regarded as a detrimental load that reduces the pile's axial capacity and is likely to exceed the pile's structural strength (Poulos, 1997).

Both long-term field test schemes (Bjerrum et al., 1969; Fellenius, 1972; Hong et al., 2015; Indraratna et al., 1992; Leung et al., 1991) and small-scale model tests (Lam et al., 2009; Ng et al., 2008; Shibata et al., 1982; Zhao et al., 2022) have been conducted on the development of drag load and down drag of piles. The results showed that during consolidation, the change of the effective stress in the soils governs the load transfer mode from the soil to the pile, which controls the magnitude of the drag load, down drag as well as the position of the neutral plane (NP, the position where no relative movement takes place between the pile and the surrounding soil). In addition, only a few millimeters of relative displacement are needed to fully mobilise the skin friction in both negative and positive directions.

In addition, numerical simulations have been conducted using various soil constitutive models (Chiou and Wei, 2021; Lee et al., 2002; Liu et al., 2012; Sun et al., 2015; Zhao et al.,

2022) and pile-soil interface models (Alonso et al., 1984; Cao et al., 2014; Chen et al., 2009; Jeong et al., 2004; Yan et al., 2012) to study the NSF on piles. Chen et al. (2009) developed a hyperbolic interface model and investigated the distribution of the NSF and axial force considering the nonlinear consolidation. Yan et al. (2012) proposed a modified algorithm in subroutine which can consider the effect of excess pore pressure in the pile-soil interface behaviour. Chiou and Wei (2021) used the modified Cam Clay model to simulate soft soil and verified their findings by field test results. The influence of pile head loading, surcharge pressure and different types of bearing layers on the drag load were analyzed properly.

Although the consolidation of soft soil has been considered in simulations of the time-dependent development of the drag load, the existing literature has overall neglected the viscous behaviour of soft soil, such as creep. Nevertheless, the creep deformation of clay is intrinsic to soft soils and should be considered in engineering design (Chen et al., 2021; Yin and Graham, 1994; Yin and Zhu, 2020). Creep induced settlements can influence the development of drag load, especially over the entire course of design life, for example, 50 years (HKIE, 2017). Notably, even assuming that the settlement due to creep accounts for a small percentage of the total settlement, it should be noted that only a few millimeters could fully mobilise the NSF as mentioned earlier. Furthermore, the creep deformation may also generate excess pore pressure (Yin and Zhu, 1999; Yin et al., 1994), influencing the load transfer from the soil to the pile. The creep effect on the development of drag load and the location of the NP are not fully understood, and research on the magnitude of drag load after long-term consolidation remains limited.

This study aims to investigate the NSF of a single pile embedded in soft soil with and without considering creep. In this paper, firstly, an elasto-viscoplastic model is used to consider the creep behaviour of the soft soil, and with the enhanced time integration algorithm the model is implemented into the finite element code ABAQUS. Then, the numerical model is established and verified through a field case. Lastly, the parametric analysis is conducted. The creep effects on NSF and NP, as well as settlement and excess pore pressure of the soil in both the primary consolidation and secondary consolidation are examined.

2. Elasto-viscoplastic model with enhanced time integration algorithm

In this study, the finite element software ABAQUS (Dassault Systemes, 2020) is employed to simulate the behaviour of the pile-soil system. Although the modified Cam Clay model (MCC) is one of the most popular models for simulating soft soil behaviour in ABAQUS (Roscoe and Burland, 1968), the MCC model takes no account of the viscous behaviour, such as creep. Therefore, the ANICREEP model that is extended from overstress theory of Perzyna proposed by Yin et al. (2010, 2011), has been selected as a representative elasto-viscoplastic model for soft clays in this study. A further introduction to the ANICREEP model is provided in **Appendix A**. This model is implemented into ABAQUS as a user-defined material via using the material subroutine UMAT. UMAT will be called at all Gauss integration points of elements through which the ANICREEP is implemented. For each calculation step, stresses and state variables have to be updated, and the material Jacobian matrix is calculated and provided for the stiffness matrix of the element.

Katona (1984) put forward an algorithm for elasto-viscoplastic models using a time

integration scheme. To enhance the algorithm, the original Katona algorithm with adaptive substepping (OK-AS) is briefly introduced in **Appendix B**. Since OK-AS failed to consider the hardening parameters changing with viscoplastic strain in the iterative procedure, the convergence rate is significantly reduced. Therefore, in order to improve the robustness of the ANICREEP model and calculation performance in the finite element analysis, the modified Katona algorithm with adaptive substepping (MK-AS) is applied for the stress-strain-time integration. Both the stress and the hardening parameters are changing with viscoplastic strain in the iterative procedure simultaneously. Submitting **Eq. (B1)** and **Eq. (B2)** into **Eq. (B5)**, the equation could be rearranged as:

$$\bar{\boldsymbol{P}}(\boldsymbol{\sigma}', \boldsymbol{\zeta}, \dot{\boldsymbol{\varepsilon}}^{vp}) = \bar{\boldsymbol{Q}}_0 \tag{1}$$

where

$$\begin{cases} \bar{\boldsymbol{P}} = \begin{bmatrix} \boldsymbol{D}^{-1}\boldsymbol{\sigma}' + \Delta t\theta\dot{\boldsymbol{\varepsilon}}^{vp} \\ \boldsymbol{\zeta} - \Delta t\theta\dot{\lambda}\boldsymbol{h} \end{bmatrix} \\ \bar{\boldsymbol{Q}}_0 = \begin{bmatrix} \Delta\boldsymbol{\varepsilon} - \Delta t(1-\theta)\dot{\boldsymbol{\varepsilon}}_0^{vp} + \boldsymbol{D}^{-1}\boldsymbol{\sigma}_0' \\ \boldsymbol{\zeta}_0 + \Delta t(1-\theta)\dot{\lambda}_0\boldsymbol{h}_0 \end{bmatrix} \end{cases} \tag{2}$$

where $\boldsymbol{\sigma}'$ are the stress vectors, $\boldsymbol{\zeta}$ are the hardening parameters, $\dot{\boldsymbol{\varepsilon}}^{vp}$ is the viscoplastic strain rate, $\boldsymbol{D}$ is the elastic matrix, Δt is the time increment, $\dot{\lambda}$ is the viscoplastic multiplier, θ is the adjustable integration parameter, $\boldsymbol{h}$ are the hardening parameters.

The flow chart of MK-AS is shown in **Fig. 1**. The modified viscoplastic strain rate $\dot{\boldsymbol{\varepsilon}}^{vp}$ is updated based on new stress $\boldsymbol{\sigma}'$ and hardening parameters $\boldsymbol{\zeta}$. $\boldsymbol{\sigma}'$ and $\boldsymbol{\zeta}$ can be calculated following the Newton-Raphson procedure. The MK-AS shows more rigorous procedures than

OK-AS and can be applied in this study. Besides, different from Wang et al. (2022), the implicit integration scheme (i.e., $\theta = 1$) is used in this study, with the advantages of high accuracy, robust integration and unconditional stability of the implicit algorithm (Yin et al., 2019, Zhang et al., 2022). Substepping parameters k is set to 0.01. The convergence criterion *TOL* is given as 0.001, which is considered appropriate for most engineering calculations (Solan 1987, Feng 2016).

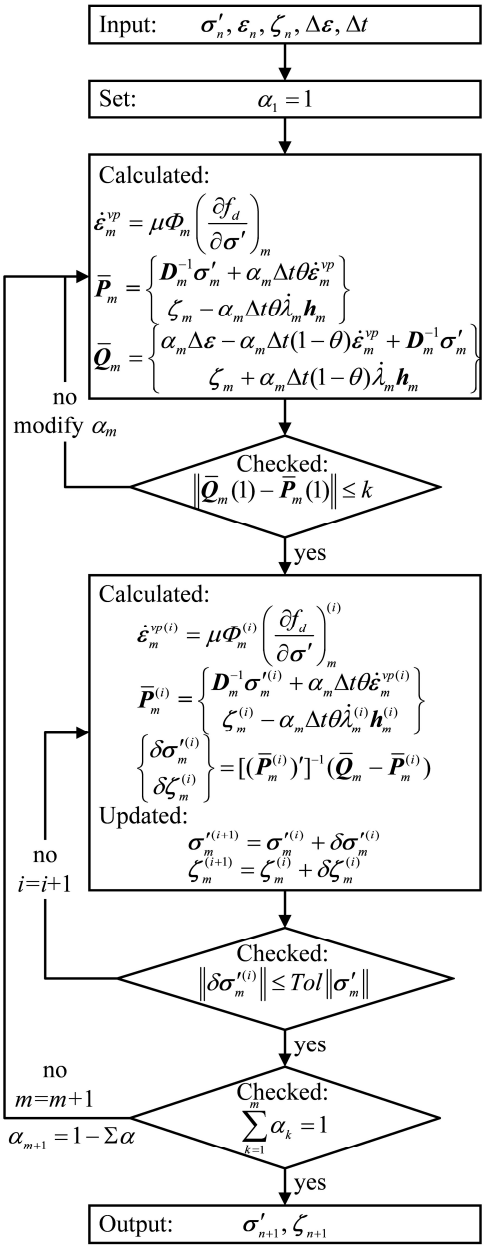

Fig. 1 Modified Katona Algorithm with adaptive substepping procedure.

3. Numerical model for negative skin friction

3.1 Brief introduction of Field test

Indraratna et al. (1992) carried out a field test in stratified soils to investigate the development of NSF in driven piles and settlement of the soil surface after the construction of an embankment. The test site was located in Bangkok city. The sub-soils were mainly thick layered marine clay, including a weathered clay layer with a thickness of approximately 2-4 m, a thick soft clay layer with a thickness of approximately 16 m, a medium stiff to still clay layer with a thickness of about 6-8 m and then following the sand layer. The groundwater table was located at 1.5-2 m below the original ground surface. The soft clay was slightly over consolidated whereas the top layer of soil had an overconsolidation ratio (OCR) of 3. Through the field investigation, the coefficient of earth pressure ranged from 0.6 to 0.75.

Two types of instrumented piles, coated pile (pile treated with bitumen coated thin layer) and uncoated pile (pile without bitumen coated thin layer), were tested. The length of the piles was 27 m, while the outer and inner diameters of the piles were 0.4 and 0.25 m, respectively. After the piles were installed by drop hammer, there remained 2 m of pile length above the ground surface. Then an embankment of 2 m height was built within 3 days. The long-term monitoring of ground surface settlement and pile axial loading was performed for 265 days.

3.2 Model parameters

In the field test, the distance between the two tested piles is 10 m (25 times of pile diameter), which is large enough to ignore the pile group effect and boundary effect (Liang et al., 2021).

Therefore, the single pile-soil interaction model is considered as two-dimensional axisymmetric. The sketch and mesh detail of the verification model is shown in **Fig. 2**. The size of the model is 10 m × 42 m. The minimum distance from the pile to the boundary is more than 10 times the pile diameter, which is considered large enough to reduce the boundary effect (Sun et al., 2015). The four-node bilinear axis-symmetric finite elements (CAX4 for pile, embankment and soil above the groundwater level; CAX4P for soil under the groundwater level, which is assumed to be fully saturated) are adopted in mechanical-flow coupled consolidation analysis (Dassault Systemes, 2020). The mesh is denser near the pile and coarser far away from the pile to avoid the influence of the stress concentration and enhance the calculation efficiency. The vertical boundary on the left side is the symmetrical line, the roller boundary and the fixed boundary are applied on the side and bottom of the model, respectively. To simplify the field case, pile is assumed wished-in-place rather than being driven (Lee et al., 2002; Hanna et al., 2006; Yan et al., 2012; Liu et al., 2012; Sun et al., 2015; Chiou et al., 2021).

The friction behaviour between soil and pile follows the Coulomb friction law, in which the shear stress is proportional to the relative shear displacement; additionally, the shear stress becomes stable after reaching the threshold displacement. The two governed parameters, are the frictional parameter, μ=0.3, estimated by $\mu=\tan(2/3\varphi_c)$ where soil effective friction angle is, φ_c=25°, and threshold displacement, δ=3 mm, which are adopted following Lee et al. (2002) and Yan et al. (2012).

In the original Coulomb friction model in ABAQUS, the normal stress was the total stress rather than effective stress, even in fluid-coupled cases (Yan et al., 2012). Therefore, a modified

Coulomb friction model considering effective stress as normal stress is developed using the user subroutine, FRIC, following Yan et al. (2012) and ABAQUS Manual (Dassault Systemes, 2020). In the model verification procedure, the geostatic step is calculated first to generate the initial stress of each stratum. After the geostatic equilibrium, the embankment is activated and applied on the top of ground surface in mechanical-consolidation coupled analysis step. Then the excess pore pressure will dissipate within the assigned time period in the consolidation stage. The drainage boundaries are placed at the ground water table and the top of the sand layer.

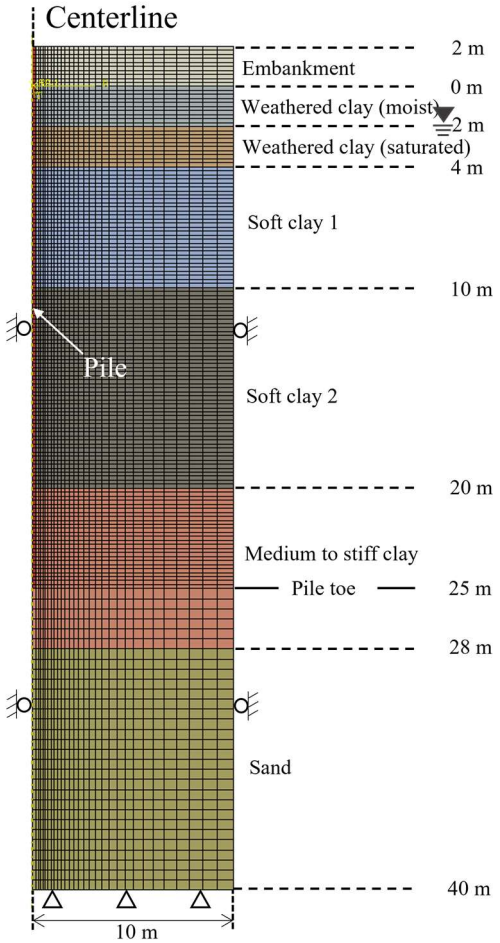

Fig. 2 Sketch and mesh detail of the verification model (4525 elements for soil, 272 elements for pile and 330 elements for embankment).

160 The isotropic linear elastic model is applied for modelling the embankment, pile and end
161 bearing sand layer. A solid pile rather than a hollow pile is used, the equilibrium elastic modulus
162 of the solid pile is calculated to maintain the same axial rigidity compared with the hollow pile.
163 The ANICREEP model is used for capturing the creep behaviour of soft soil. Compared with
164 the modified Cam Clay model used in the previous studies (Chiou and Wei, 2021; Indraratna
165 et al., 1992; Liu et al., 2012; Yan et al., 2012), the additional parameters, such as creep
166 coefficient $C_{\alpha e}$, initial bonding ratio χ_0, absolute rate of bond degradation ξ, relative rate of
167 bond degradation ξ_d, need to be determined in the ANICREEP model. According to Yin et al.
168 (2011), the initial bonding ratio χ_0 can be obtained by the oedometer test or shear vane test
169 between the undisturbed and remolded soil; the absolute rate of bond degradation ξ and relative
170 rate of bond degradation ξ_d can be determined based on the curve fitting from one-dimensional
171 and isotropic compression test. The detailed explanation is given in **Appendix. A**. It is
172 noteworthy that the soil structure has pronounced effect on the development of NSF. It has been
173 proved that the increasing of the soil initial bonding amount decreases the shaft friction of the
174 pile (Li and Li, 2021). Since the structure of clays in the selected case study was not reported,
175 and additionally, the field soil can be generally estimated as a type of slightly structured soil
176 (Horpibulsuk et al., 2007), it is reasonable to ignore the interparticle bonding and debonding
177 effects in simulations.

178 $C_{\alpha e}$ is the key parameter for the applicability of elasto-viscoplastic constitutive model in
179 practical engineering, which can be determined by the oedometer test. However, $C_{\alpha e}$ was not
180 reported for the studied case as well. Some empirical correlations between $C_{\alpha e}$ and the physical

properties of soft soils (such as void ratio, water content, plastic limit and liquid limit) have been proposed in previous research (Nakase and Kamei, 1986; Suneel et al., 2008; Yin, 1999; Zhu et al., 2016). The empirical equations for $C_{\alpha e}$ were for reconstituted clay instead of intact clay; hence, the destruction effect on creep was excluded and could be better applicated to engineering practice (Mesri and Godlewski, 1977; Yin and Karstunen, 2011). Notably, these empirical equations are only appropriate to a few specific clays. Through the evolutionary polynomial regression method, Jin et al. (2019) found that $C_{\alpha e}$ to be highly correlated with void ratio, plasticity index and liquid limit, and put forward a reliable method to predict the $C_{\alpha e}$. This method is applied in this study, as shown in Eq. (3):

$$\ln(C_{\alpha e}) = \left(0.055\frac{1}{w_L^2 I_p} - 0.107\frac{1}{I_p^2} + 0.272(\frac{w_L}{I_p})^2 \right) e - 2.222 \quad (3)$$

where e is the void ratio, I_p is the plasticity index and w_L is the liquid limit.

Other parameters, such as the saturated unit weight γ, swelling index κ, compression index λ, slope of critical state line in p'-q (mean effective stress - deviatoric stress) plane M, elastic modulus E are the same as those adopted by Indraratna et al. (1992). The overconsolidation ratio OCR, coefficient of earth pressure K_0, Poisson's ratio v, initial void ratio e_0 are obtained based on the interpretation of field measured data in Indraratna et al. (1992). Noted that Yan et al. (2012) and Chiou and Wei (2021) enlarged the permeability coefficients, k, 10 times larger than the data from ground measurement to better fit the field test result, due to the limitations of drainage condition in the site and inhomogeneity of soil. Thus, the same k is adopted in this study. The details of parameters for the verification case are summarized in **Table 1**.

Table 1 Summary of parameters for verification case study.

Material type	Depth m	γ kN/m^3	κ	λ	M	e_0	k (10^{-4}) m/day	OCR	K_0	v	$C_{\alpha e}$	E kN/m^2
Soil												
Embankment	-2-0	16.7	-	-	-	-	-	-	0.4	0.2	-	4900
Weather clay (moist)	0-2	16.7	0.053	0.182	1.05	1.54	-	2.7	0.7	0.33	0.01	-
Weather clay (saturated)	2-4	16.7	0.053	0.182	1.05	1.54	67.6	2.7	0.7	0.33	0.01	-
Soft clay 1	4-10	14.7	0.084	0.514	0.97	2.46	5.5	1.2	0.6	0.33	0.021	-
Soft clay 2	10-20	16.7	0.063	0.323	0.98	1.55	2.63	1.3	0.6	0.33	0.007	-
Medium to stiff clay	20-28	18.6	0.027	0.116	0.9	1.2	3.72	1.8	0.67	0.33	0.004	-
Sand	28-40	19.1	-	-	-	-	67.6	-	0.45	0.33	-	27440
Pile												
Pile	-2-25	14.7	-	-	-	-				0.33	-	30×10^6

3.3 Validation results

The finite element calculation results of the uncoated pile are compared with the field test data. **Fig. 3(a)** offers a comparison between the observed settlement and the simulated settlement of soils. The measured distance is 0.25 m away from the pile center line. The numerical results can well predict the soil settlement with time after applied surcharge load. The settlement of each depth continues to increase with consolidation and soil creep. However, Yan et al. (2012) 's simulation results underestimated the soil settlement after consolidation for 50 days, the difference between the calculated and field obtained settlement also increased with time, owing to the exclusion from consideration of the creep deformation. Accordingly, the creep effect must be taken into account in the long-term settlement analysis of soft soil.

The development of pile axial force at various times after embankment construction (i.e., 3, 25, 156 and 256 days) is shown in **Fig. 3(b)** along with monitored data. The calculated axial

force is in general agreement with the overall time-varying trend of field data, except for some discrepancies. The axial force increases with the proceeding of consolidation as expected. **Fig. 3(c)** reveals the varying tendency of unit skin friction along the pile shaft obtained from axial force with elapsed time. The compared field data of unit skin friction is only displayed after 265 days of embankment load. In the figure, the NSF and positive skin friction (PSF) indicate the downward and upward friction direction, respectively. With the increase of consolidation degree, the PSF gradually reverses to NSF around the pile head due to the increase in relative displacement. The PSF also increases with time around the pile toe because of the pile settlement induced by down drag. The NSF (or PSF) is small near the NP due to the small relative displacement and the skin friction is not totally mobilised (i.e., the relative displacement is within 3 mm). The NP moves downward and then locates at approximately 18 m below the original ground surface, which is quite similar to the field measured position.

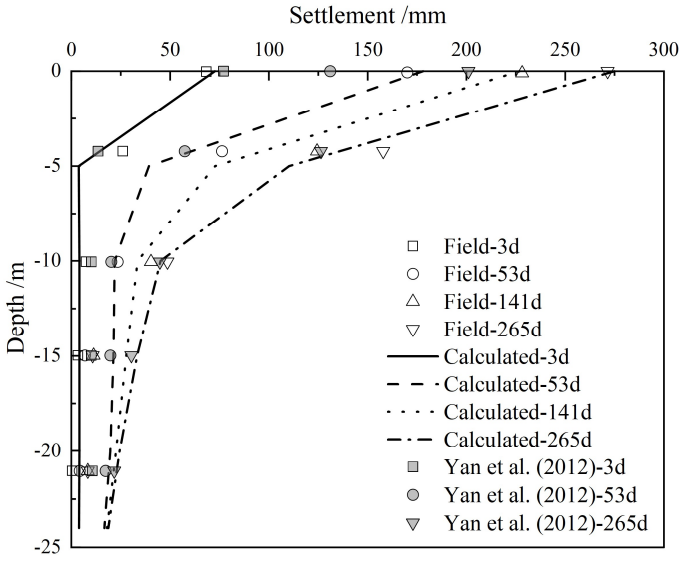

(a)

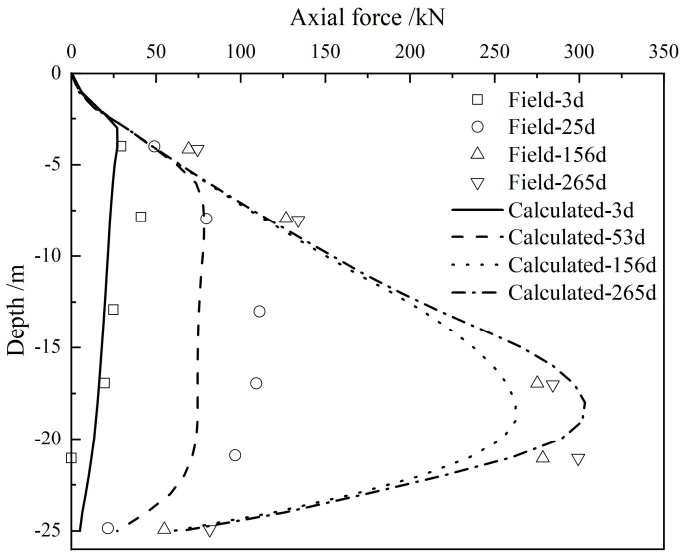

(b)

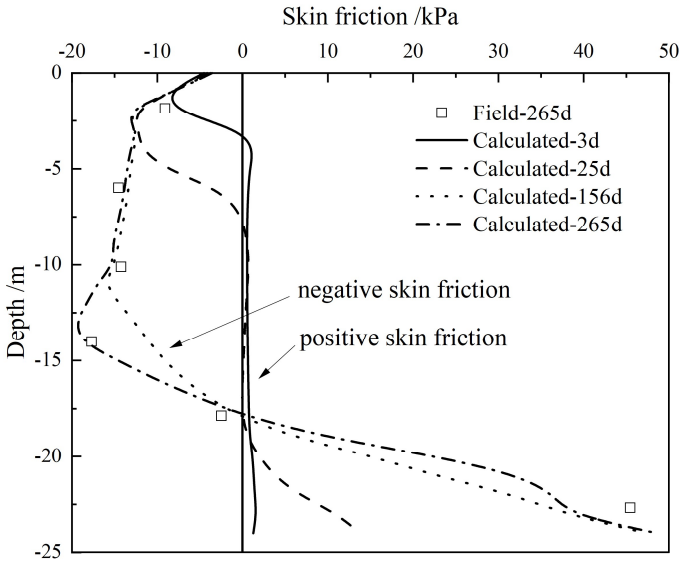

(c)

Fig. 3 Calculated results of the verification model compared with field measure data: (a) soil ground settlement; (b) axial force; (c) negative skin friction ('d' represents days).

3.4 Model for parametric analysis

According to the comparison results discussed previously, the established verification model is able to capture the growing trend of NSF and soil settlement. Thus, further investigation of the creep effect on NSF, is pursued by building a simplified numerical model for parametric analysis, as shown in **Fig. 4**. Following the same modelling approach, the ground water table is located at the ground level. The solid pile with the diameter of 0.4 m and the

length of 25 m is fully embedded in the consolidating layer. The bearing layer is 5 m high with the same soil property as the consolidating layer. The ANICREEP model is applied in both consolidating and bearing layers. **Table 2** summarizes the parameters of the pile and soil layer.

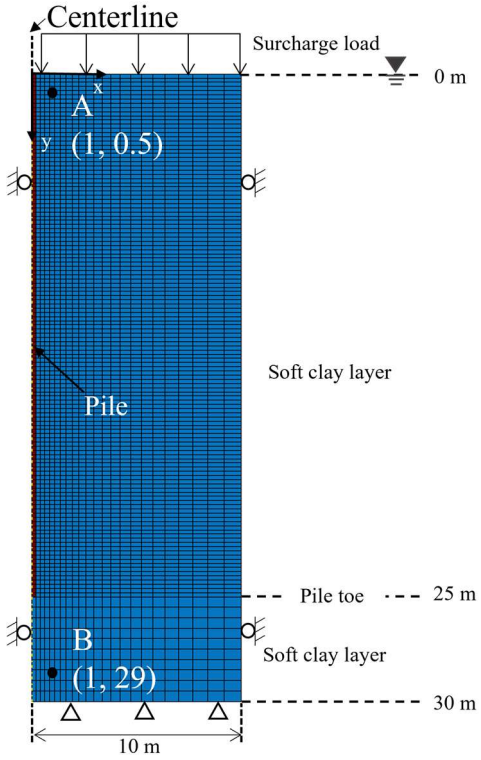

Fig. 4 Sketch and mesh for the parametric study model.

Table 2 Parameters of soft clay and pile in parametric analysis model.

Material type	Depth m	γ kN/m^3	κ	λ	M	e_0	k (10^{-4}) m/day	OCR	K_0	v	$C_{\alpha e}$	E kN/m^2
Soil												
Soft clay	0-30	16.7	0.063	0.323	0.98	1.55	9	1	0.6	0.3	0.01	-
Pile												
Pile	0-25	14.7	-	-	-	-				0.3	-	30×10^6

Unless otherwise stated, parameters and analysis steps in the parametrical model are the same as aforementioned validation model. The friction coefficient, μ=0.3 and the threshold displacement, δ=3 mm are applied in the soil-pile interaction behaviour. The drainage boundary

is set at the ground surface. The embankment load of 34 kPa is applied within 3 days. The consolidation process starts after the application of the surcharge load.

Taking the massive experimental data collected by Jin et al. (2019), the relationship between the creep coefficient, $C_{\alpha e}$, and void ratio, e, of various types of clay is plotted in **Fig. 5**. The $C_{\alpha e}$ is ranged from 0.001 to 0.02, except from some scattered data up to 0.023. In the parametric analysis part, the benchmark value of $C_{\alpha e}$ can be adopted as 0.01, estimated by the average $C_{\alpha e}$ of each clay layer in the verification case study. Comparing with the benchmark value, $C_{\alpha e}$ =0.001 and $C_{\alpha e}$ =0.02, represent the lower and higher creep effect, respectively, elicited from **Fig. 5.**

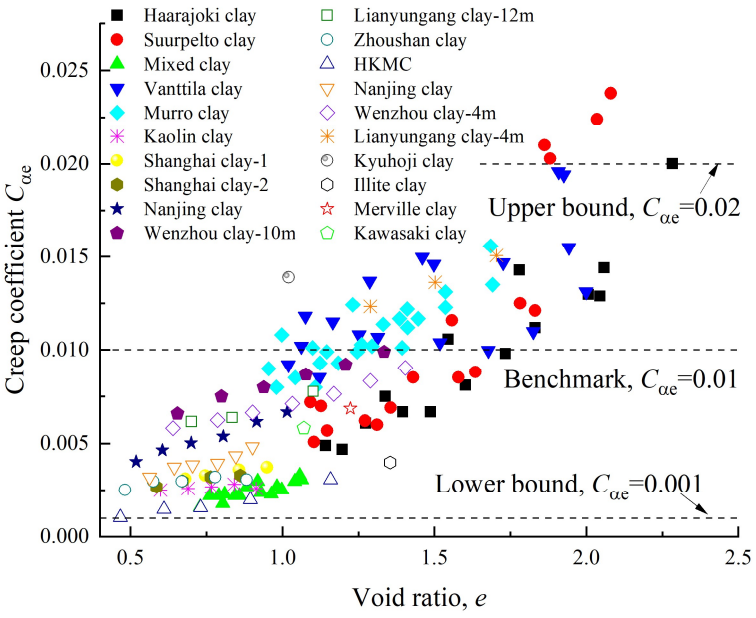

Fig. 5 Creep coefficient of various clays.

Due to the convergence problem during calculation, a very low value (i.e., 1% of the benchmark $C_{\alpha e}$) of $C_{\alpha e}$ is considered as the case without creep rather than directly setting $C_{\alpha e}$ =

0 following Wu et al. (2020). For comparison, the $C_{\alpha e}$ = 0.00001 (0.1% of the benchmark $C_{\alpha e}$) is selected to conduct the sensitivity analysis to verify the reliability of the no creep condition.

Table 3 Values of creep coefficient.

Influencing parameter	Value
Creep coefficient, $C_{\alpha e}$	0.00001 (sensitivity analysis), 0.0001 (no creep), 0.001, 0.01 (benchmark), 0.02

4. Parametric analysis results

4.1 Creep effect on settlement

The development of ground settlement at point A (1m away from pile center line) with time is shown in **Fig. 6**. The larger settlement is observed under higher creep effect, as expected. The settlement exceeds 3.7 m when $C_{\alpha e}$ = 0.02, which is more than triple the results calculated without creep. In addition, the relationship between vertical strain ε_{yy} and vertical effective stress (log scale) $\log\sigma'_{yy}$ at point A with various $C_{\alpha e}$ is also depicted in **Fig. 7**. The creep effect is observed compared with no creep. Greater $C_{\alpha e}$, is associated with a higher creep strain rate, resulting in a more significant creep behaviour. Two tangent lines are utilized in **Fig. 6** to estimate the consolidation rate following Casagrande's method (Casagrande, 1936). As the figure demonstrates, consolidation rate of soft soil layer decreases with the increase of $C_{\alpha e}$. Furthermore, it should be noted that this method is used to reflect the creep effect on consolidation rate rather than indicating the time when creep occurred. Through the sensitivity analysis, it concludes that $C_{\alpha e}$ =0.0001 (1% of the benchmark $C_{\alpha e}$) has the same results compared with $C_{\alpha e}$ =0.00001 (0.1% of the benchmark $C_{\alpha e}$), indicating that a further reduction

in creep coefficient does not affect the settlement results. Therefore, it is reasonable to choose the 1% of benchmark $C_{\alpha e}$ to represent the no creep condition.

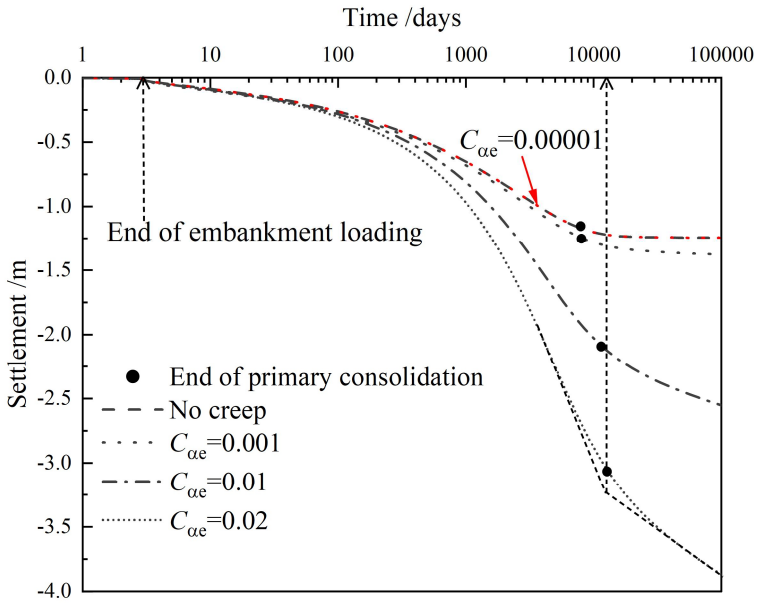

Fig. 6 Development of ground settlement with various creep parameters versus time (No creep: 1% of the benchmark $C_{\alpha e}$).

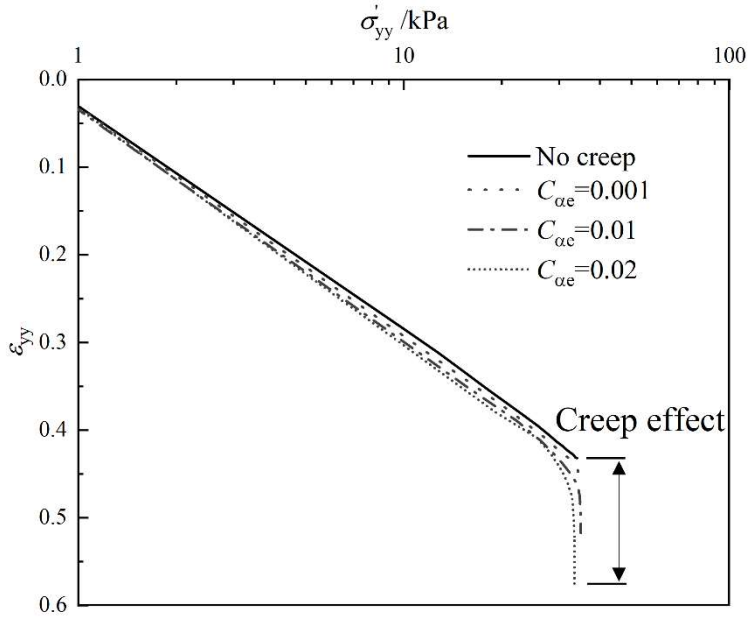

Fig. 7 The relationship between vertical strain ε_{yy} and vertical effective stress $\log\sigma'_z$ with various $C_{\alpha e}$.

4.2 Creep effect on excess pore pressure

Point B in **Fig. 4** is selected to observe the change in excess pore pressure (Δu). **Fig. 8** reflects the calculation results of Δu over time with and without creep. There shows a significant increase in Δu after the end of embankment load due to the creep effect compared with the calculation results excluding creep. This increase in Δu is due to the drainage of water from micropores in the microstructure into the macrostructure (Yin et al., 1994). As for the higher creep case, when consolidation begins, increasing rate of Δu induced by plastic volumetric strain on account of creep effect is higher than the decreasing rate of Δu due to dissipation, and hence the Δu shows the increasing trend. When the creep induced increasing rate of Δu is lower than the decreasing rate of Δu during the consolidation process, the Δu reaches the peak value and then gradually decreases until being totally dissipated.

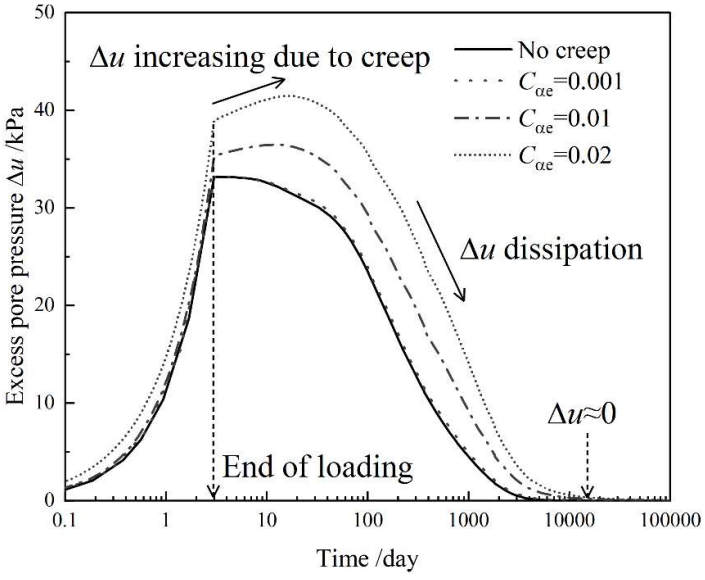

Fig. 8 The changing of excess pore pressure over time at point B.

4.3 Creep effect on negative skin friction

The creep effect on the development of drag load and skin friction along the pile with consolidation time up to 50 years is investigated and the results are presented in **Fig. 9**. As

expected, with the increasing of consolidation time, the drag load and NSF continue increasing and a higher drag load is observed with a greater creep coefficient. The fully mobilised NSF reveals the approximately linear variation with depth on account of the linear increase in vertical effective stress in this study.

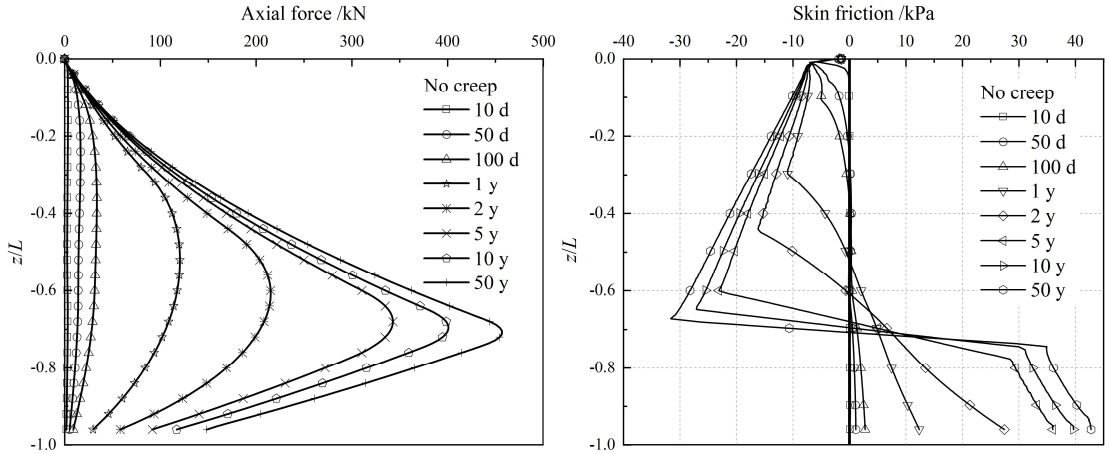

(a) No creep

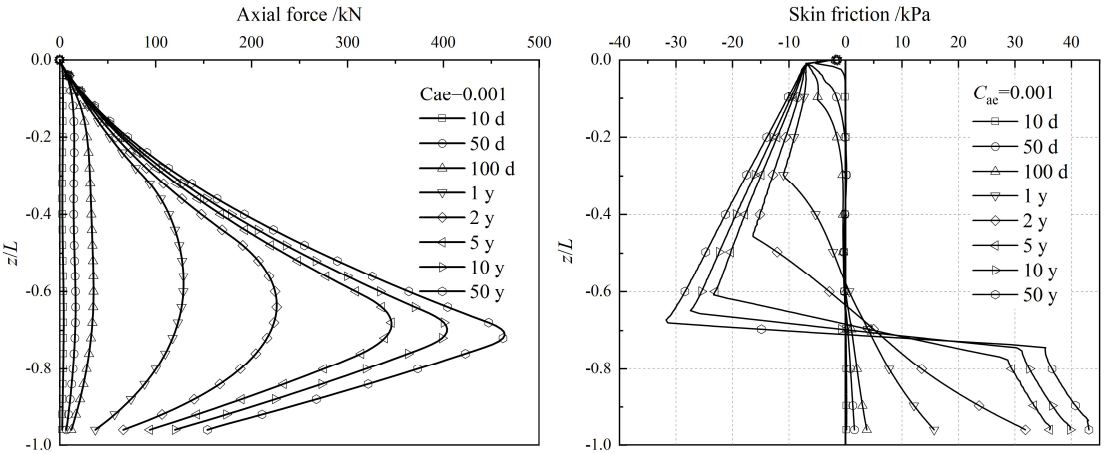

(b) $C_{\alpha e}$=0.001

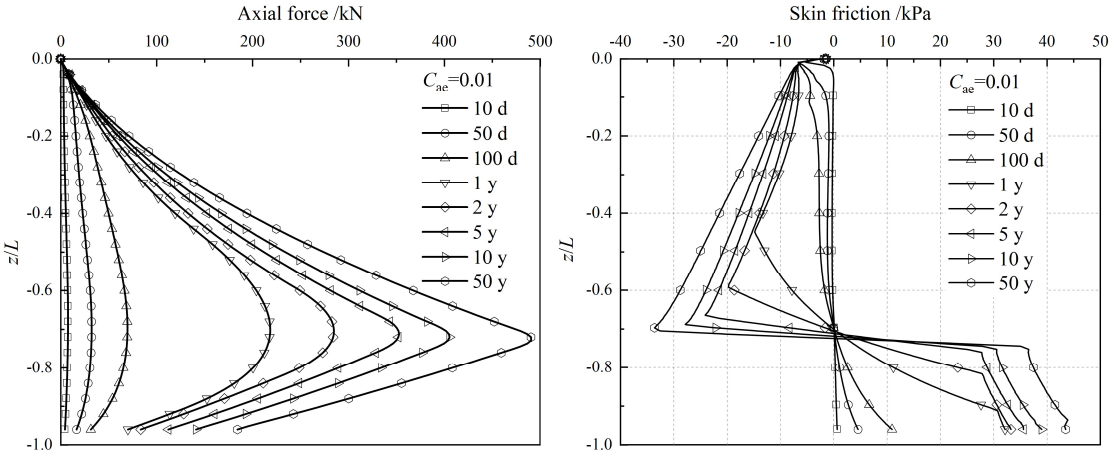

(c) C_{ae}=0.01

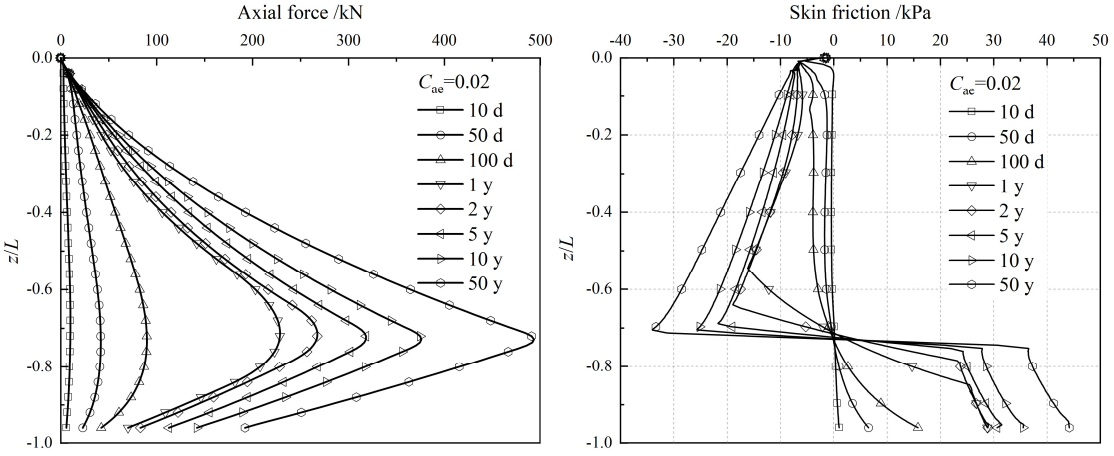

(d) C_{ae}=0.02

Fig. 9 Distribution of drag load and negative skin friction with time: (a) no creep; (b) C_{ae}=0.001; (c) C_{ae}=0.01; (d) C_{ae}=0.02. ('d' and 'y' represent days and years, respectively).

In order to study the creep effect on NSF with consolidation, the dimensionless time T_{Uc} is used, in which the subscript U_c represents the degree of consolidation. For example, T_{Uc}=1 indicates the time when primary consolidation (U_c=100%) is reached. When $0 \leqslant T_{Uc} \leqslant 1$ denotes the time period in primary consolidation, T_{Uc}>1 indicates the time in "secondary consolidation". A relationship between the normalized drag load $P/P_{Tuc=1}$ and T_{Uc} with or without creep is established, as shown in **Fig. 10**, where P denotes the drag load at the NP, $P_{Tuc=1}$ signifies the drag load after full dissipation of excess pore pressure.

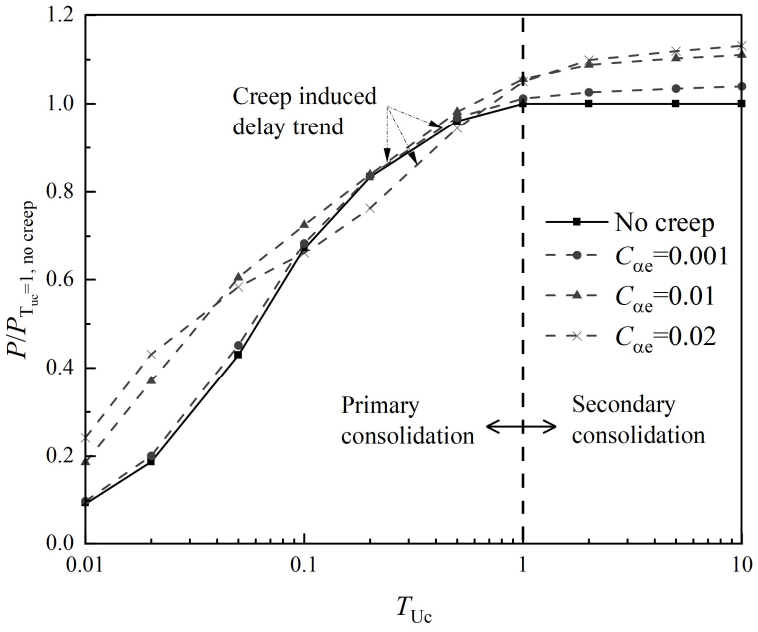

Fig. 10 Changing of drag load with consolidation degree with or without creep.

For the case where the creep effect is ignored, the drag load, P increases with time during the primary consolidation and then becomes stable. Whereas, for the cases considering creep, there will still be an increase in P due to the on-going settlement caused by creep. At the initial stage of consolidation, higher P is observed with the increase of creep coefficient. During the middle period of consolidation, the lower increasing rate of P is observed compared with no creep case, as well as a significant delay in P increment with higher creep effect. This phenomenon is mainly attributed to the creep induced excess pore pressure as explained in the previous section, which decreased the effective stress around the pile. According to the Coulomb friction interface model adopted in this study, the decrease of normal contact effective stress reduces the shear force at clay-pile interface. At the later period of consolidation, a higher increasing rate of P re-appears with a higher creep coefficient.

In practice, the effective stress related β method (Burland, 1973; Johannessen and Bjerrum,

1965) can be used to calculate the skin friction along the pile as follows:

$$f_s = \beta \sigma'_v \tag{4}$$

where f_s is the shaft friction and σ'_v is the effective vertical stress. The drag load at the NP can be calculated based on the following equation:

$$P_{\text{drag, NP}} = \pi D \int_0^{L_{\text{NP}}} f_s dz \tag{5}$$

where L_{NP} and D are the depth of the NP and the pile diameter, respectively. Therefore, the back-analyzed β can be calculated during the primary and secondary consolidation periods.

Fig. 11 illustrates the development of the dimensionless β value ($\beta/\beta_{\text{Tuc=1, no creep}}$) where $\beta_{\text{Tuc=1, no creep}}$ is the back-calculated value after primary consolidation ignoring creep. At the beginning of consolidation, the no creep case shows the higher β value compared with creep cases because of the lower descending rate of the NP, where the effective stress is relatively low. With the development of consolidation, the β value increases until the end of primary consolidation. Similar findings were reported in both field tests (Hong et al., 2015; Indraratna et al., 1992) and centrifuge tests (Lam et al., 2013; Ng et al., 2008). When considering creep, a higher dimensionless β value is obtained, which increases to 1.05 after primary consolidation and to 1.13 when T_{uc}=10 for the case with the biggest creep coefficient.

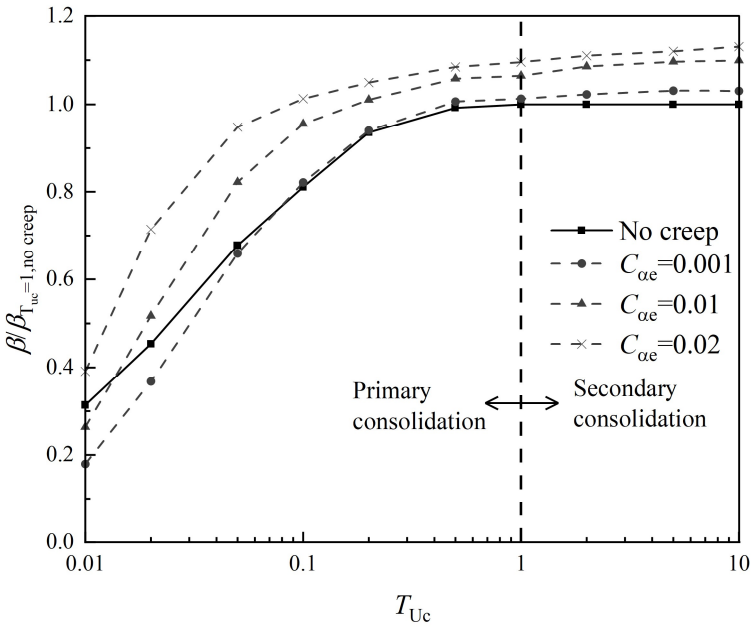

357

358 **Fig. 11 Change in drag load with consolidation degree with or without creep.**

359 **4.4 Creep effect on neutral plane**

360 The position of NP describes the depth where soil and pile settle equally, which is also the
361 location where the maximum drag load is generated along the pile. The variation of NP position
362 with consolidation time is inferred from skin friction as shown in **Fig. 12**. For convenience, the
363 NP depth is expressed as normalized depth L_{NP}/L_0, where the L_{NP} is the depth from the NP to
364 the soil surface, L_0 is the pile embedded length. Observably, following the full dissipation of
365 excess pore pressure, the NP position is stable in both the no creep and creep cases. Therefore,
366 in the results, the study focused on NP variation in primary consolidation.

367 The variation tendency of NP position can be generally divided into two phases, namely
368 Phase 1 and Phase 2. For the no creep case, in Phase 1, there is an upward trend in L_{NP}/L_0, the
369 value of which reaches 0.64 within 10% degree of primary consolidation. In Phase 2, the value
370 of L_{NP}/L_0 shows steady upward, which rises to 0.70 at the final stage. For the creep cases, a

371 sharp increase in the NP position at the initial time can be found in Phase 1. The inflection time
372 $T_{uc,s}$ (the definition is shown in **Fig. 13** and will be discussed later) also shows a great decrease
373 with higher creep effect. In Phase 2, NP is much closer to a steady state but demonstrates a
374 slight increase with time. Furthermore, an increase in creep coefficient shifts NP slightly
375 downward.

376 For comparison, theoretical predictions of NP position based on different methods from
377 the literature are presented in **Fig. 12**. Alonso et al. (1984) developed a stress-transfer method
378 to describe the interaction behaviour between the pile and soil induced by NSF. The design
379 chart for NP position with various conditions is proposed. The NP is located at L_{NP}/L_0=0.7,
380 with zero pile toe resistance and no pile head loading. NAVFAC (1986) suggested that the value
381 of L_{NP}/L_0 can be estimated as 0.75 if there is no available test data. Bowles (1988) presented a
382 simple design method to locate the NP considering the surcharge load. The calculated NP is
383 about 0.67. The Chinese national standard provided the empirical value for the NP in the light
384 of pile tip surrounding soil. The suggested NP location L_{NP}/L_0 is 0.5-0.6 for the pile-tip soil in
385 clay or silt.

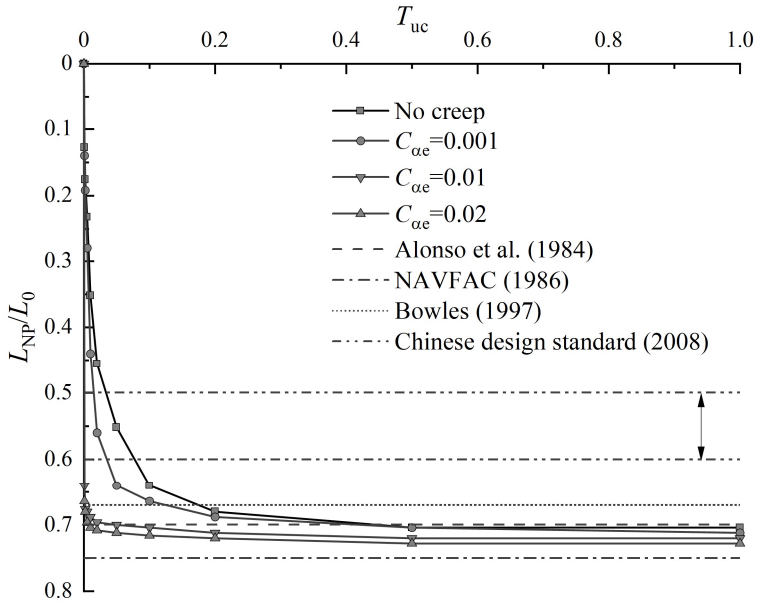

386

387 **Fig. 12 Relationship between the neutral plane position with time.**

388 It can be seen that the result provided by Alonso et al. (1984) shows consistency with the
389 NP position ignoring creep, although it is a special case that neglects the toe resistance
390 mobilization. Other empirical methods have yielded either overestimated or underestimated
391 results, implying that these methods are uneconomical and conservative. These methods also
392 failed to consider the time dependence of the NP. To address this issue, the exponential function
393 to describe the variation of NP position with time was proposed by Zhang et al. (2022) and
394 validated by field monitoring results. The prediction results show a higher correlation
395 relationship compared with the hyperbolic model provided Cao et al. (2014). Therefore, the
396 improved exponential function is applied to analyze the creep effect on the NP position, as
397 shown below:

398 $$\frac{L_{NP}}{L_0} = a\left(1 - e^{-kT_{uc}^{b}}\right) \tag{6}$$

399 where L_{NP}/L_0 and T_{uc} are the normalized NP position and consolidation time as mentioned

above; meanwhile, a, b and k are the fitting controlling factors, where a is the NP value at the steady state, k and b control the variation rate of the NP. Based on the variation rate of NP, Phase 1 and Phase 2 can be divided by $T_{uc,s}$, where θ is half of the angle composed by the intersection of asymptotic line at the initial and end of the fitting curve, as shown in **Fig. 13**.

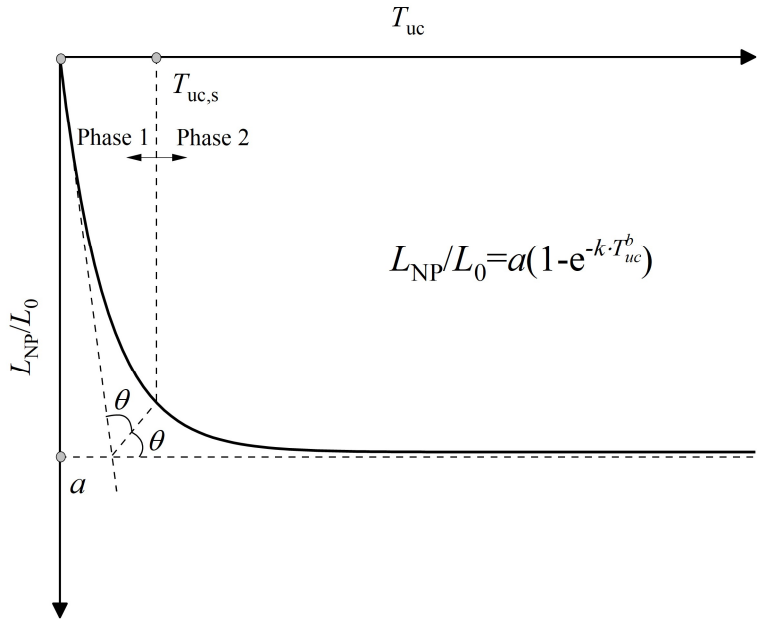

Fig. 13 Exponential prediction model for NP position.

Fig. 14 reveals the fitting results of the exponential model, as well as the fitting parameters and correlation coefficient, R^2. The adopted model is able to accurately predict the NP position with time considering creep. Nevertheless, these fitting parameters are controlled by site conditions, such as surcharge load, pile head loading, the properties of consolidation, end bearing layer, creep effect, pile size and pile-soil interface friction, etc.. Furthermore, the site condition varies from one project to another. Future work is needed to find a more sophisticated method to consider the coupling effect of all influencing parameters.

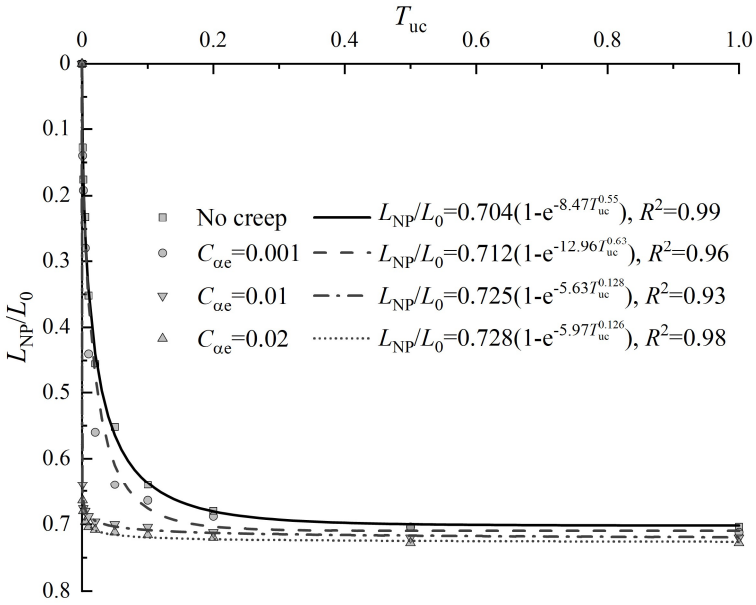

Fig. 14 Fitting results of the exponential model.

5. Conclusions

In this study, an elasto-viscoplastic model adopting an enhanced time integration algorithm with higher calculation robustness was successfully implemented into ABAQUS through user subroutine UMAT. This model was firstly employed to simulate a known field test with the verification. Then, an in-depth investigation of the creep effect on the NSF and NP in the primary and secondary consolidation period was thoughtfully conducted. The resulting detailed findings and conclusions are drawn as follows:

(1) When compared with the non-creep case, it shows a higher drag load as well as back-calculated β value after primary consolidation when considering creep, because more soil settlement results in higher relative displacement between the soil and pile, which further mobilizing the NSF.

(2) The creep induced delay trend on drag load is observed with higher creep effect during

primary consolidation procedure. In line with the Coulomb-friction interface law, the skin friction is proportional to normal effective stress, and therefore, the generation of extra excess pore pressure caused by creep deformation impedes the development of effective stress in the clay-pile interface, leading to the lower drag load.

(3) The value of normalized NP position (L_{NP}/L_0) starts at 0 and increases to around 0.7 after consolidation when ignoring creep, which is similar to the special case calculated by Alonso et al. (1984). The location of NP moves downward when considering creep, though a limited downward trend is observed as the increasing of creep effect. A sharp descent of the NP position can be observed at the beginning of consolidation at a higher level of creep effect of the surrounding soil.

(4) The current empirical formula can neither predict the NP position well nor consider its time dependency. In contrast, an improved exponential prediction model with three controlling parameters is presented and applied to predict the variation of NP position with time considering creep effect.

In this study, the pile driven procedure is ignored. Pile driven causes significant disturbance within the soil around the pile shaft, which leads to the changes of stress state in the surrounding soil. The generation of the excess porewater pressure during pile penetration may take long time to entirely dissipate. Further study will be conducted in the future to analyze the pile driven effect to properly apply these findings into field driven piles.

Acknowledgements

This research was financially supported by the Research Grants Council (RGC) of Hong Kong Special Administrative Region Government (HKSARG) of China (RIF: R5037-18; GRF: 15210020l).

Data Availability Statement

All data that support the findings of this study are available from the corresponding author upon reasonable request.

Conflict of Interest Statement

We declare that we have no known competing financial interests or personal relationships that could have appeared to influence the work reported in this article.

Appendix A: Brief introduction of ANICREEP model

Based on Yin et al. (2011), the main constitutive equations are listed as follows (**Fig. A1**):

$$\dot{\varepsilon}_{ij} = \dot{\varepsilon}_{ij}^{e} + \dot{\varepsilon}_{ij}^{vp} \tag{A1}$$

$$\dot{\varepsilon}_{ij}^{vp} = \mu \left(\frac{p_m^d}{p_m^r} \right)^{\beta} \frac{\partial f_d}{\partial \sigma'_{ij}} \tag{A2}$$

$$f_r = \frac{\frac{3}{2}\left(\sigma_d'^r - p'^r \alpha_d\right) : \left(\sigma_d'^r - p'^r \alpha_d\right)}{\left(M^2 - \frac{3}{2}\alpha_d : \alpha_d\right) p'^r} + p'^r - p_m^r = 0 \tag{A3}$$

$$d\alpha_d = \omega \left[\left(\frac{3\sigma_d}{4p'} - \alpha_d \right) \left\langle d\varepsilon_v^{vp} \right\rangle + \omega_d \left(\frac{\sigma_d}{3p'} - \alpha_d \right) d\varepsilon_d^{vp} \right] \tag{A4}$$

$$p_m^r = (1+\chi)\, p_{mi} \tag{A5}$$

$$dp_{mi} = p_{mi} \left(\frac{1+e_0}{\lambda_i - \kappa} \right) d\varepsilon_v^{vp} \tag{A6}$$

$$d\chi = -\chi\xi \left(\left| d\varepsilon_v^{vp} \right| + \xi_d d\varepsilon_d^{vp} \right) \tag{A7}$$

where $\dot{\varepsilon}_{ij}$ denotes the (i , j) component of the total strain rate tensor, and the superscripts e and vp represent, respectively, the elastic and the viscoplastic components. The $p_m{}^d$ is the size of the dynamic loading surface. The $p_m{}^r$ and p_{mi} are the size of the reference and the intrinsic yield surfaces respectively. The initial reference preconsolidation pressure σ'^r_{p0} obtained from an oedometer test can be used as an input to calculate the initial size p_{m0} using Eq.(A3).

The slope of the critical state line M is expressed as follows:

$$M = M_c \left[\frac{2c^4}{1 + c^4 + (1 - c^4)\sin 3\theta} \right]^{\frac{1}{4}} \tag{A8}$$

where $c = (3 - \sin\phi_c) / (3 + \sin\phi_c)$ according to the Mohr-Coulomb yield criterion (ϕ_c is the friction angle); $-\pi/6 \le \theta = (1/3)\sin^{-1}\left(-3\sqrt{3}\bar{J}_3 / 2\bar{J}_2^{3/2}\right) \le \pi/6$ using $\bar{J}_2 = (1/2)\bar{s}_{ij} : \bar{s}_{ij}$, $\bar{J}_3 = (1/3)\bar{s}_{ij}\bar{s}_{jk}\bar{s}_{ki}$ with $\bar{s}_{ij} = \sigma_d - p'\alpha_d$.

Soil constants and state variables are summarized in Table A1 with their recommended methods of determination.

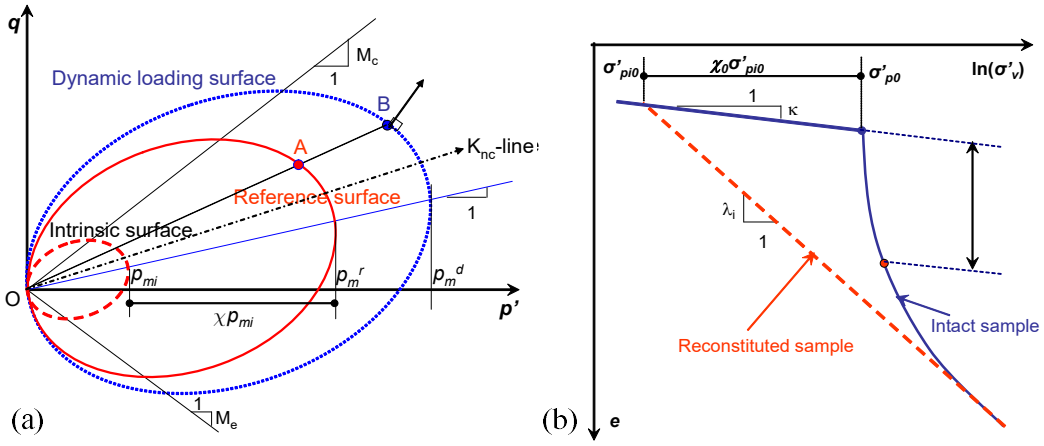

478

479 **Fig. A1 Definitions for the model in (a) *p*'- *q* space; and (b) one-dimensional compression condition**

480 **Table A1. State parameters and soil constants of elastic viscoplastic model**

Group	Parameter	Definition	Determination
Modified Cam Clay parameters	σ'^{r}_{p0}	Initial reference preconsolidation pressure	From a selected oedometer test whose loading-rate is used as reference strain-rate
	e_0	Initial void ratio (state parameter)	From oedometer test
	υ'	Poisson's ratio	From initial part of stress-strain curve (Typically varying from 0.15 to 0.35)
	κ	Slope of the swelling line	From 1D or isotropic consolidation test
	λ_i	Intrinsic slope of the compression line	From 1D or isotropic consolidation test
	M	Slope of the critical state line	From triaxial shear test
Anisotropy parameters	α_0	Initial anisotropy (state parameter for calculating initial components of the fabric tensor)	$\alpha_0=\alpha_{K0}=\eta_{K0}-\frac{M^2-\eta_{K0}^2}{3}$ with $\eta_{K0}=\frac{3M}{6-M}$
	ω	Absolute rate of yield surface rotation	$\omega=\frac{1+e_0}{(\lambda_i-\kappa)}\ln\frac{10M_c^2-2\alpha_{K0}\omega_d}{M_c^2-2\alpha_{K0}\omega_d}$
Destructuration parameters	χ_0	Initial bonding ratio	$\chi_0=S_t-1$ (from shear vane test), or $\chi_0=\sigma'_{p0}/\sigma'_{pi0}-1$ (from oedometer tests)
	ξ	Absolute rate of bond degradation	From consolidation tests with two different stress ratios η=q/p', e.g. oedometer test and isotropic consolidation test
	ξ_d	Relative rate of bond degradation	
Viscosity parameters	$C_{\alpha ei}$	Secondary compression coefficient	From 24h oedometer test on reconstituted sample
Hydraulic parameters	k_{v0}, k_{h0}	Initial vertical and horizontal permeability	From oedometer tests
	c_k	Permeability coefficient	From curve e-log(k)

481

Appendix B: Brief introduction of Original Katona algorithm with adaptive substepping

In one loading step with strain increment $\Delta\boldsymbol{\varepsilon}$ ($\Delta\boldsymbol{\varepsilon}=\boldsymbol{\varepsilon}_{n+1}-\boldsymbol{\varepsilon}_n$) and time increment Δt ($\Delta t = t_{n+1}-t_n$), where the n denotes the number of loading steps, the effective stress increment $\Delta\boldsymbol{\sigma}'$ and hardening parameter $\Delta\boldsymbol{\zeta}$ of the ANICREEP model can be expressed as:

$$\Delta\boldsymbol{\sigma}' = \boldsymbol{D}(\Delta\boldsymbol{\varepsilon}-\Delta\boldsymbol{\varepsilon}^{vp}) \tag{B1}$$

$$\Delta\boldsymbol{\zeta} = \Delta\lambda\boldsymbol{h} \tag{B2}$$

$$\boldsymbol{\zeta} = \left[p_{ci} \;\; \chi \;\; \boldsymbol{\alpha}_{\mathrm{d}}\right]^T \tag{B3}$$

$$\boldsymbol{h} = \begin{bmatrix} p_{ci}\dfrac{1+e_0}{\lambda_i-\kappa}\dfrac{\partial f_d}{\partial p'} \\ -\chi\xi\left(\left|\dfrac{\partial f_d}{\partial p'}\right|+\xi_d\dfrac{\partial f_d}{\partial q}\right) \\ \omega\left[\left(\dfrac{3\boldsymbol{\sigma}_d}{4p'}-\boldsymbol{\alpha}_d\right)\left\langle\dfrac{\partial f_d}{\partial p'}\right\rangle+\omega_d\left(\dfrac{\boldsymbol{\sigma}_d}{3p'}-\boldsymbol{\alpha}_d\right)\dfrac{\partial f_d}{\partial q}\right] \end{bmatrix} \tag{B4}$$

where $\boldsymbol{\sigma}'$ and $\boldsymbol{\varepsilon}$ are the stress and strain vectors respectively, can be expressed as $\boldsymbol{\sigma}'=[\sigma_x',\sigma_y',\sigma_z',\tau_{xy},\tau_{yz},\tau_{zx}]^T$ and $\boldsymbol{\varepsilon}=[\varepsilon_x,\varepsilon_y,\varepsilon_z,\gamma_{xy},\gamma_{yz},\gamma_{zx}]^T$, $\Delta\boldsymbol{\varepsilon}^{vp}$ are the elasto-viscoplastic strain increment vectors, $\boldsymbol{D}$ is the elastic matrix, $\Delta\lambda$ is the viscoplastic multiplier.

In order to apply the ANICREEP model into the finite element software, the step-by-step time integration scheme proposed by Katona (1984) is used, the time dependent strain increment is determined by:

$$\Delta\boldsymbol{\varepsilon}^{vp} = \Delta t\left[(1-\theta)\dot{\boldsymbol{\varepsilon}}_0^{vp}+\theta\dot{\boldsymbol{\varepsilon}}^{vp}\right] \tag{B5}$$

where $\dot{\boldsymbol{\varepsilon}}_0^{vp}$ are the known viscoplastic strain vectors, Δt is the time increment, θ is the adjustable integration parameter, in the range from $0\leqslant\theta\leqslant1$, when θ=0 is the full explicit

500 method, $0<\theta<1$ is the semi-implicit method, when $\theta=1$ is the implicit method. Submitting **Eq.**

501 **(B1)** into **Eq. (B5)**, the equation could be rearranged as:

502 $$\boldsymbol{P}(\boldsymbol{\sigma}^{'},\ \dot{\boldsymbol{\varepsilon}}^{vp}) = \boldsymbol{Q}_0 \tag{B6}$$

503 where

504 $$\begin{cases} \boldsymbol{P} = \boldsymbol{D}^{-1}\boldsymbol{\sigma}^{'} + \Delta t\theta\dot{\boldsymbol{\varepsilon}}^{vp} \\ \boldsymbol{Q}_0 = \Delta\boldsymbol{\varepsilon} - \Delta t(1-\theta)\dot{\boldsymbol{\varepsilon}}_0^{vp} + \boldsymbol{D}^{-1}\boldsymbol{\sigma}^{'} \end{cases} \tag{B7}$$

505 The flow chart of original Katona algorithm with adaptive substepping (OK-AS) is shown

506 in **Fig. B1**, where the *TOL* represents the convergence criterion used to judge iterative

507 convergence and the superscript *i* denotes the i^{th} iteration.

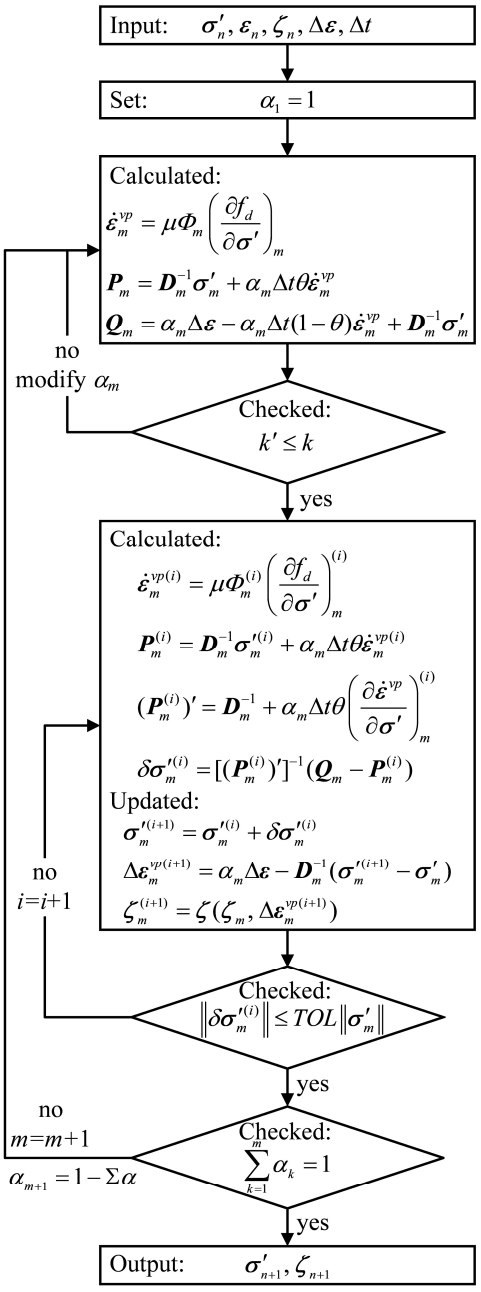

Fig. B1 Flow chart of original Katona algorithm with adaptive substepping procedure

References

Alonso, E., Josa, A. Ledesma, A. (1984). Negative skin friction on piles: a simplified analysis and prediction procedure. Géotechnique, 34(3), 341-357.

Bjerrum, L., Johannessen, I. Eide, O. (1969). Reduction of negative skin friction on steel piles to rock. Proceedings of the Seventh International Conference on Soil Mechanics and Foundation Engineering,

Bowles, J. E. (1988). Foundation analysis and design.

Burland, J. (1973). Shaft friction of piles in clay--a simple fundamental approach. 6(3), 30-38.

Cao, W., Chen, Y. Wolfe, W. (2014). New load transfer hyperbolic model for pile-soil interface and negative skin friction on single piles embedded in soft soils. International Journal of Geomechanics, 14(1), 92-100.

Casagrande, A. (1936). The determination of the preconsolidation load and its practical significance. Proceedings of the International conference on soil mechanics and foundation engineering,

Chen, R., Zhou, W. Chen, Y. (2009). Influences of soil consolidation and pile load on the development of negative skin friction of a pile. Computers and Geotechnics, 36(8), 1265-1271.

Chen, Z.-J., Feng, W.-Q. Yin, J.-H. (2021). A new simplified method for calculating short-term and long-term consolidation settlements of multi-layered soils considering creep limit. Computers and Geotechnics, 138, 104324.

Chiou, J.-S. Wei, W.-T. (2021). Numerical investigation of pile-head load effects on the negative skin friction development of a single pile in consolidating ground. Acta Geotechnica, 16(6), 1867-1878.

Dassault Systemes. (2020). ABAQUS analysis user's manual version 2020.

Fellenius, B. H. (1972). Down-drag on piles in clay due to negative skin friction. Canadian Geotechnical Journal, 9(4), 323-337.

Fellenius, B. H. (1989). Unified design of piles and pile groups. Transportation Research Record, 1169, 75-82.

Feng, W. (2016). Experimental study and constitutive modelling of the time-dependent stress-strain behavior of soils. PhD dissertation, The Hong Kong Polytechnic University.HKIE. (2017). Code of practice for foundations.

Hong, Y., Ng, C. W. W., Chen, Y., Wang, L. Chan, V. (2015). Field study of downdrag and dragload of bored piles in consolidating ground. Journal of Performance of Constructed Facilities, 4015050.

Horpibulsuk, S., Shibuya, S., Fuenkajorn, K., & Katkan, W. (2007). Assessment of engineering properties of Bangkok clay. Canadian Geotechnical Journal, 44(2), 173-187.

547 Indraratna, B., Balasubramaniam, A., Phamvan, P. Wong, Y. (1992). Development of negative
548 skin friction on driven piles in soft Bangkok clay. Canadian Geotechnical Journal, 29(3),
549 393-404.

550 Jeong, S., Lee, J. Lee, C. J. (2004). Slip effect at the pile–soil interface on dragload. Computers
551 and Geotechnics, 31(2), 115-126.

552 Jin, Y.-F., Yin, Z.-Y., Zhou, W.-H., Yin, J.-H. Shao, J.-F. (2019). A single-objective EPR based
553 model for creep index of soft clays considering L2 regularization. Engineering Geology,
554 248, 242-255. https://doi.org/https://doi.org/10.1016/j.enggeo.2018.12.006

555 Johannessen, I. Bjerrum, L. (1965). Measurement of the compression of a steel pile to rock due
556 to settlement of the surrounding clay. Proceedings of the sixth International Conference
557 on Soil Mechanics and Foundation Engineering,

558 Katona, M. G. (1984). Evaluation of viscoplastic cap model. Journal of Geotechnical
559 Engineering, 110(8), 1106-1125.

560 Lam, S., Ng, C. W., Leung, C. F. Chan, S. (2009). Centrifuge and numerical modeling of axial
561 load effects on piles in consolidating ground. Canadian Geotechnical Journal, 46(1), 10-
562 24.

563 Lam, S. Y., Ng, C. W. W. Poulos, H. G. (2013). Shielding Piles from Downdrag in
564 Consolidating Ground. Journal of Geotechnical and Geoenvironmental Engineering,
565 139(6), 956-968. https://doi.org/10.1061/(asce)gt.1943-5606.0000764

566 Lee, C. J., Bolton, M. D. Al-Tabbaa, A. (2002). Numerical modelling of group effects on the
567 distribution of dragloads in pile foundations. Géotechnique, 52(5), 325-335.
568 https://doi.org/10.1680/geot.2002.52.5.325

569 Leung, C. F., Radhakrishnan, R. Tan, S.-A. (1991). Performance of precast driven piles in
570 marine clay. Journal of Geotechnical Engineering, 117(4), 637-657.

571 Li, L., Li, J. (2021). Analysis of Shaft Resistance Setup of Driven Piles in Soft Sensitive Clays
572 Considering Soil Consolidation and Creep. International Journal of Geomechanics, 21(11),
573 04021216.

574 Liang, R., Yuan, Y., Fu, D., Liu, R. (2021). Cyclic response of monopile-supported offshore
575 wind turbines under wind and wave loading in sand. Marine Georesources &
576 Geotechnology, 39(10), 1230-1243.

577 Liu, J., Gao, H. Liu, H. (2012). Finite element analyses of negative skin friction on a single
578 pile. Acta Geotechnica, 7(3), 239-252.

579 Mesri, G. Godlewski, P. M. (1977). Time-and stress-compressibility interrelationship. Journal
580 of the Geotechnical Engineering Division, 103(5), 417-430.

581 Nakase, A. Kamei, T. (1986). Influence of strain rate on undrained shear characteristics of K0-
582 consolidated cohesive soils. Soils and Foundations, 26(1), 85-95.

583 NAVFAC. (1986). Foundations and earth structures.

584 Ng, C. W., Poulos, H. G., Chan, V. S., Lam, S. S. Chan, G. C. (2008). Effects of tip location
585 and shielding on piles in consolidating ground. Journal of Geotechnical and
586 Geoenvironmental Engineering, 134(9), 1245-1260.

587 Poulos, H. (1997). Piles subjected to negative friction: A procedure for design. Geotechnical
588 Engineering, 28, 23-44.

589 Roscoe, K. H. Burland, J. (1968). On the generalized stress-strain behaviour of wet clay.

590 Shibata, T., Sekiguchi, H. Yukitomo, H. (1982). Model test and analysis of negative friction
591 acting on piles. Soils and Foundations, 22(2), 29-39.

592 Sloan, S. (1987). Substepping schemes for the numerical integration of elastoplastic stress–
593 strain relations. International journal for numerical methods in engineering, 24(5), 893-
594 911.

595 Sun, T., Yan, W. Su, D. (2015). Fully coupled consolidation analysis of shear strength
596 mobilization and dragload of a pile subject to negative skin friction. International Journal
597 of Geomechanics, 15(3), 04014057.

598 Suneel, M., Park, L. K. Im, J. C. (2008). Compressibility characteristics of Korean marine clay.
599 Marine Georesources and Geotechnology, 26(2), 111-127.

600 Wang, H., Li, L., Li, J. (2022). A simple stress correction method for explicit integration
601 algorithm of elastoplastic constitutive models and its application to advanced anisotropic
602 S-CLAY1 model. Computers and Geotechnics, 148, 104817.

603 Wu, P.-C., Feng, W.-Q. Yin, J.-H. (2020). Numerical study of creep effects on settlements and
604 load transfer mechanisms of soft soil improved by deep cement mixed soil columns under
605 embankment load. Geotextiles and Geomembranes, 48(3), 331-348.
606 https://doi.org/https://doi.org/10.1016/j.geotexmem.2019.12.005

607 Yan, W. M., Sun, T. K. Tham, L. G. (2012). Coupled-consolidation modeling of a pile in
608 consolidating ground. Journal of Geotechnical and Geoenvironmental Engineering,
609 138(7), 789-798.

610 Yin, J.-H. (1999). Properties and behaviour of Hong Kong marine deposits with different clay
611 contents. Canadian Geotechnical Journal, 36(6), 1085-1095.

612 Yin, J.-H. Graham, J. (1994). Equivalent times and one-dimensional elastic viscoplastic
613 modelling of time-dependent stress–strain behaviour of clays. Canadian Geotechnical
614 Journal, 31(1), 42-52.

615 Yin, J.-H. Zhu, G. (2020). Consolidation analyses of soils. CRC Press.

616 Yin, J.-H. Zhu, J.-G. (1999). Elastic viscoplastic consolidation modelling and interpretation of
617 pore-water pressure responses in clay underneath Tarsiut Island. Canadian Geotechnical
618 Journal, 36(4), 708-717.

619 Yin, J., Graham, J., Clark, J. I. Gao, L. (1994). Modelling unanticipated pore-water pressures
620 in soft clays. Canadian Geotechnical Journal, 31(5), 773-778.

621 Yin, Z.-Y., Chang, C. S., Karstunen, M. Hicher, P.-Y. (2010). An anisotropic elastic–
622 viscoplastic model for soft clays. International Journal of Solids and Structures, 47(5),
623 665-677.
624 Yin, Z.-Y. Karstunen, M. (2011). Modelling strain-rate-dependency of natural soft clays
625 combined with anisotropy and destructuration. Acta Mechanica Solida Sinica, 24(3), 216-
626 230.
627 Yin, Z. Y., Karstunen, M., Chang, C. S., Koskinen, M. Lojander, M. (2011). Modeling Time-
628 Dependent Behavior of Soft Sensitive Clay. Journal of Geotechnical and
629 Geoenvironmental Engineering, 137(11), 1103-1113.
630 https://doi.org/10.1061/(asce)gt.1943-5606.0000527
631 Yin, Z. Y., Li, J., Jin, Y. F., Liu, F. Y. (2019). Estimation of robustness of time integration
632 algorithms for elasto-viscoplastic modeling of soils. International Journal of
633 Geomechanics, 19(2), 04018197.
634 Zhang, Q., Wang, Z.-Y., Yin, Z.-Y., Jin, Y.-F. (2022). A novel stabilized NS-FEM formulation
635 for anisotropic double porosity media. Comput. Methods Appl. Mech. Engrg. 401, 115666.
636 https://doi.org/10.1016/j.cma.2022.115666.
637 Zhang, X., Liu, X., Chang, Z., Liu, Z., Yu, D. Li, Y. (2022). Time Dependence of Neutral Plane
638 Position in a PHC-Supported Soft Subgrade. Journal of Geotechnical and
639 Geoenvironmental Engineering, 148(2), 05021016.
640 Zhao, Z., Ye, S., Zhu, Y., Tao, H. Chen, C. (2022). Scale model test study on negative skin
641 friction of piles considering the collapsibility of loess. Acta Geotechnica, 17(2), 601-611.
642 Zhu, Q.-Y., Yin, Z.-Y., Hicher, P.-Y. Shen, S.-L. (2016). Nonlinearity of one-dimensional creep
643 characteristics of soft clays. Acta Geotechnica, 11(4), 887-900.
644